iScience

CellPress
OPEN ACCESS

Article

Constructing N-doped and 3D Hierarchical Porous graphene nanofoam by plasma activation for supercapacitor and Zn ion capacitor

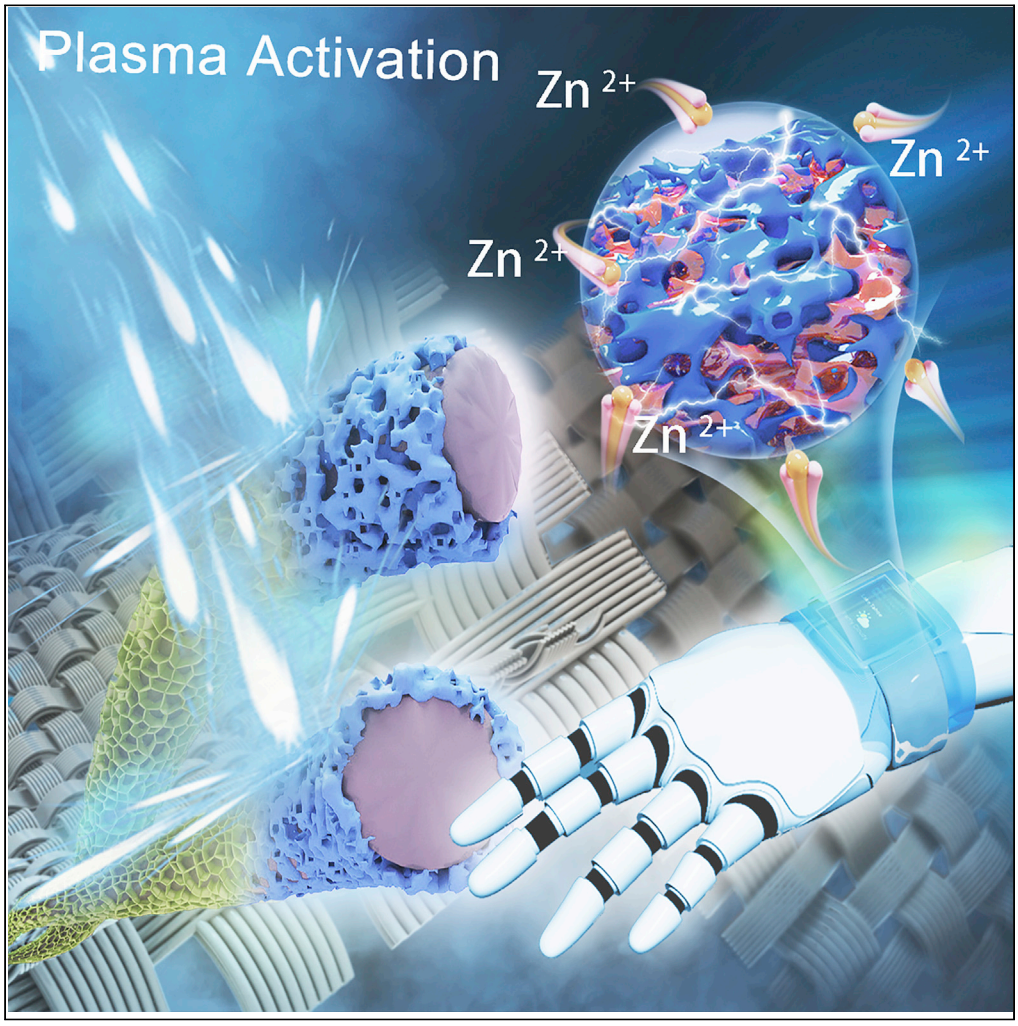

Song Wei, Caichao Wan, Xingong Li, Jiahui Su, Wenjie Cheng, Huayun Chai, Yiqiang Wu

wancaichaojy@163.com (C.W.)
wuyq0506@126.com (Y.W.)

Highlights

N-doped and 3D porous graphene nanofoam was prepared by N_2 plasma activation

N-GNF has rich active sites and micro/mesoporous nanoarchitecture

N-GNF@CFs based ZIC exhibits enhanced electrochemical properties

Wei et al., iScience 26, 105964
February 17, 2023
https://doi.org/10.1016/j.isci.2023.105964

iScience

CellPress
OPEN ACCESS

Article

Constructing N-doped and 3D Hierarchical Porous graphene nanofoam by plasma activation for supercapacitor and Zn ion capacitor

Song Wei,[1,2] Caichao Wan,[1,2,3,*] Xingong Li,[1] Jiahui Su,[1] Wenjie Cheng,[1] Huayun Chai,[1] and Yiqiang Wu[1,*]

SUMMARY

Traditional electrode materials still face vital challenges of few active sites, low porosity, complex synthesis process, and low specific capacitance. Herein, N-doped and 3D hierarchical porous graphene nanofoam (N-GNF) is created on carbon fibers (CFs) by employing a facile, fast, and environmentally friendly strategy of N_2 plasma activation. After an appropriated N_2 plasma activation, the graphene nanosheets (GNSs) synthesized by Ar/CH_4 plasma deposition transform into N-GNF successfully. N doping donates rich active sites and increases the hydrophilia, while hierarchical nanoarchitecture exposes an enlarged effective contact area at the interface between electrode and electrolyte and affords sufficient space for accommodating more electrolytes. The as-assembled flexible N-GNF@CFs//Zn NSs@CFs Zn ion capacitor delivered a high energy density of 105.2 Wh kg^{-1} at 378.6 W kg^{-1} and initial capacity retention of 87.9% at the current of 2 A g^{-1} after a long cycle of 10,000.

INTRODUCTION

Great efforts have been made to alleviate the consumption of non-renewable energy and reduce environmental pollution to meet the growing demand for green and efficient energy. It is imperative to develop appropriate energy storage and conversion technologies. Supercapacitors (SCs), delivering high power density, faster charging/discharging, and long service life through non-Faradaic and Faradaic processes in electric double-layer capacitors (EDLCs) and pseudocapacitors respectively, are considered promising candidates for efficient energy storage.[1,2] With the advantages of miniaturization and light weight, SCs can be used as power sources for various portable electronic devices such as smartphones and notebooks, even can meet the high-power output requirements for short-term acceleration in hybrid vehicles.

To date, new technologies for advanced electronics such as foldable smartphones and personal healthcare sensors require emerging developments in flexible energy storage devices as power sources. Increasing attention is paid to safety, reliability, and compatibility within the highly integrated system.[3] Therefore, flexible solid state SCs become the most promising candidates to meet these requirements due to their strong mechanical flexibility, excellent safety nature (prevents the electrolyte leakage), and nearly unchanged performance even under varying degrees of mechanical deformation.

Notwithstanding promising prospects, compared with those rechargeable batteries (such as Li, Na, or Zn ion batteries), the energy density of SC is much lower, which seriously hinders their development. An ion-hybrid capacitor, which combines the advantages of SCs and batteries, has emerged as an attractive energy storage system.[4] Among them, Zn ion capacitor (ZIC) is usually made of Zn metal as anode and carbon material as a cathode in water-based Zn ion electrolyte. With the respect to such novel energy storage devices, it is essential to create suitable cathode materials to trigger the fast electroplating/stripping kinetics onto Zn anode surfaces.

Carbon material is an ideal electrode material for SCs (including ZIC), such as activated carbon (AC), graphene or reduced graphene oxidate (rGO), and carbon nanotubes (CNTs).[5] Currently reported activated carbon materials are mainly derived from biomass pyrolysis engineering, which has the advantages of large specific surface area and low cost. However, such powdery materials often require the addition of additives

[1]College of Materials Science and Engineering, Central South University of Forestry and Technology, Changsha 410004, PR China

[2]These authors contributed equally

[3]Lead contact

*Correspondence: wancaichaojy@163.com (C.W.), wuyq0506@126.com (Y.W.)

https://doi.org/10.1016/j.isci.2023.105964

and conductive agents, which leads to a tendency for the electroactive layers to drop off the substrates under an external mechanical force or even during a long charging and discharge process, automatically reducing the charge storage efficiency and cycle life of the device. The tragic result of rGO or CNTs prepared through harsh chemical conditions and elaborate processes is that they are difficult to disperse and easy to reaccumulate, which is detrimental to the electrical conductivity and capacitive performance of electrodes. Recently, vertically oriented graphene nanosheets (GNSs) have been prepared by a plasma-enhanced chemical vapor deposition (PECVD). Compared with rGO synthesized by traditional methods, GNSs based on PECVD technology spare the limitation of aggregation and substrate of graphene sheets. Furthermore, the GNSs with a well-distributed array structure facilitate the ions to infiltrate into the electrode surface easily and quickly without using any spacers. However, untreated carbon materials (including GNSs) generally exhibit low specific capacitances that are difficult to fulfill the requirement of high energy density.

A facile and effective way to further enhance the electrochemical property of the carbon material is to tune the electronic properties of the graphite lattice by introducing heteroatoms (such as nitrogen, oxygen, sulfur, phosphorus).[6–9] It is worth noting that the artificial doping of heteroatoms, especially nitrogen (N) atoms, can effectively improve the electronic conductivity, electron-donor tendency, and surface wettability of carbon materials, and further enhance their ion/charge storage properties.[10] It has also been reported that after N doping, pseudocapacitance can be generated due to the interaction of the electrolyte with the N species on the surface, thereby enhancing the capacitive performance.[11] In addition, the construction of unique porous carbonaceous nanostructures with abundant micropores and mesopores is conducive to shortening the diffusion distance of the two ions/electrons, enabling fast transport kinetics to store more charge.[12] However, it is still challenging to create graphene materials with the integration of nitrogen doping and hierarchical porous nanostructure for high-performance SCs by facile and fast methods.

The plasma activation technology has been determined as an effective and rapid approach to carry out N doping of carbon materials to endow them with various new or enhanced properties for electrochemical applications.[13] For example, Fan and his coworkers successfully converted commercial carbon cloth into N-doped and superficial nanostructured electrode for Li-ion storage using a one-step N_2 plasma activation strategy at room temperature.[14] They found that the doping of N generated by N_2 plasma activation can improve the wettability of carbon materials, while the formation of surface nano-morphology can increase the specific surface area, which is beneficial to the ion adsorption and desorption onto the interfacial between electrode and electrolyte. According to this report, after plasma treatment, the obtained N-doped carbon cloth delivers a dramatically enlarged capacity of 391 mF cm^{-2} at 4 mA cm^{-2} than that of the untreated counterpart (0.12 mF cm^{-2}). Jeong et al. activated graphene with N_2 plasma for 3 min and achieved a maximum doping rate of 2.51% at nitrogen.[15] As a result, the N_2 plasma-induced N-doped graphene used as SC electrode shows a large capacitance of 280 F g^{-1}, much higher than that of pristine graphene without sacrificing stability and power capability. Notably, NH_3 gas is another general N source for motivating plasma activation with more active than N_2 plasma.[16] Whereas, its intense toxicity against the concept of green manufacturing. In short, the plasma activation process conducted at relatively mild conditions has irreplaceable advantages in improving the performance of energy conversion and storage materials. To the best of our knowledge, there are no SC reports involving the N-doped, 3D layered porous nanostructures using PECVD graphene as a precursor fabricated by low-temperature N_2 plasma activation, especially on a flexible carbon fiber surface, which is important for the applications in wearable electronic devices.

Herein, we proposed a combined strategy of Ar/CH_4 plasma deposition and N_2 plasma activation to create an N-doped and 3D hierarchically porous graphene foam nanostructure on the surface of CFs (N-GNF@CFs) for the enhancement of electrochemical property for SCs. The N_2 plasma activation-induced N-doping and surface structural engineering endows the PECVD graphene with multiple merits of rich N active sites, large surface area, and super-hydrophilic properties. Particularly, the elaborate design of 3D interconnected porous nanostructure greatly shortens the ion diffusion distance and strengthens the structural stability of electrodes. As a result, the as-obtained N-GNF@CFs electrode exhibits a remarkably enhanced specific capacitance of 204.2 F g^{-1} at 1 mA cm^{-2} and excellent cycling stability with a capacitance retention rate of 93.5% after 10,000 cycles. Moreover, we demonstrate a new-type flexible quasi-solid-state ZIC with large energy density and long-term durability by employing the N-GNF@CFs as a cathode and electrodeposited Zn nanosheets on

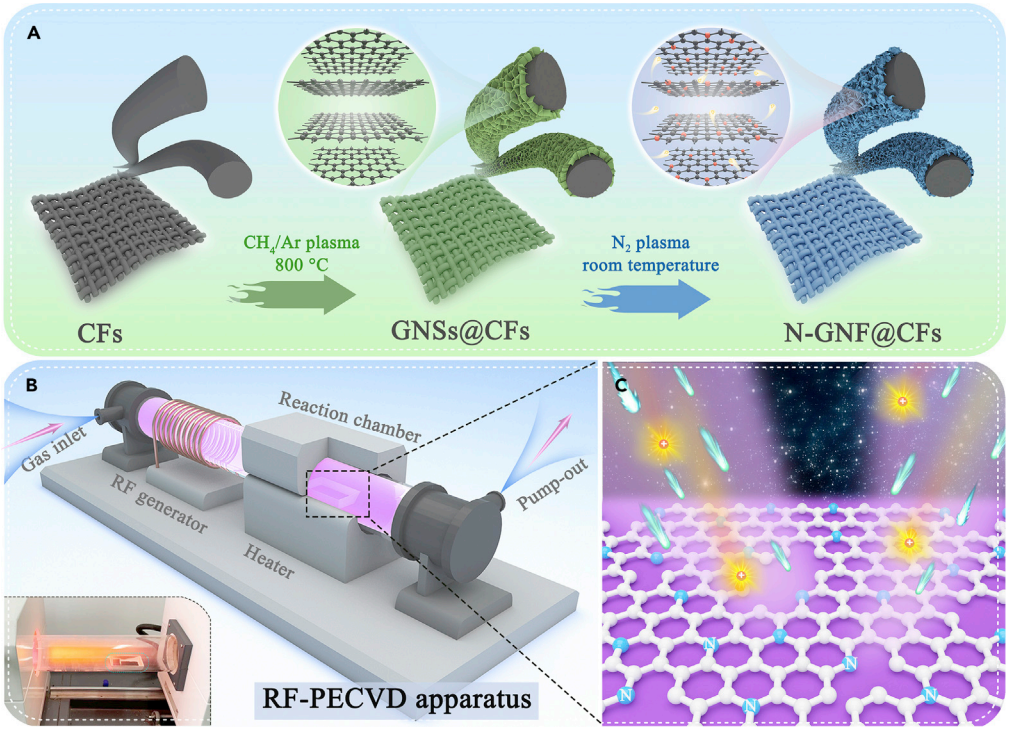

Figure 1. The design philosophy and synthetic strategy of N-GNF@CFs

(A) Fabrication processes of the N-GNF@CFs electrode.

(B) Illustration of RF-PECVD system.

(C) The mechanism diagram of the N_2 plasma activation process.

CFs (Zn NSs@CFs) as an anode. The devices displayed outstanding electrochemical performance in terms of a high capacity of 131.5 mAh g^{-1} at 0.2 A g^{-1}, an energy density of 105.2 Wh kg^{-1} at 378.6 W kg^{-1}, and extended cycle lifespan over 10,000 cycles with ~87.9% of capacitance retention.

RESULTS

Fabrication of N-GNF@CFs electrode

The design philosophy and synthetic strategy of the nanoarchitecture of N-doped and hierarchical porous graphene nanofoam encapsulating CFs are schematically illustrated in Figure 1A. The CFs with a 3D intertwined structure and rough surface (Figures S1A and S1B and supplemental information) acted as the growth matrix of graphene and were fabricated firstly by pyrolyzing cotton fabric at 1000°C. Subsequently, the vertical graphene nanosheet array was homogeneously deposited onto the surface of CFs to form a core-shell structure by Ar/CH_4 plasma in an RF-PECVD system (Figure 1B). Except for deposition reaction, plasma technology can be also applied to the surface morphology control and functionalization of various nanomaterials.[17,18] N_2 plasma has been reported to achieve nitrogen doping and nitridation in carbon and metallic oxide processing. Besides, due to the physical etching effect with a moderate-pressure discharge, N_2 plasma activation can induce the surface nanostructurization of the materials, such as surface roughness[14] and 3D interconnected meso/micropores.[18] In this article, GNSs were successfully converted into N-doped graphene nanofoam with the interconnected porous structure on the surface of CFs via an N_2 plasma activation at low temperature. As shown in Figure 1C, numerous positive ions (N_2^+/N^+) within N_2 plasma replace the partial carbon atoms of graphene to realize N doping and generate more defects.[18] On the other hand, such subtle nanostructural modification renders a large interfacial area and 3D hierarchical channels of the graphene, which is conducive to the rapid diffusion of electrolyte ions and fast transferring of electron.[19] Moreover, the N-decorated graphite carbon exhibits favorable hydrophilia and improved electrochemical activity due to its more accessible active sites and greater electron mobility.[14,20]

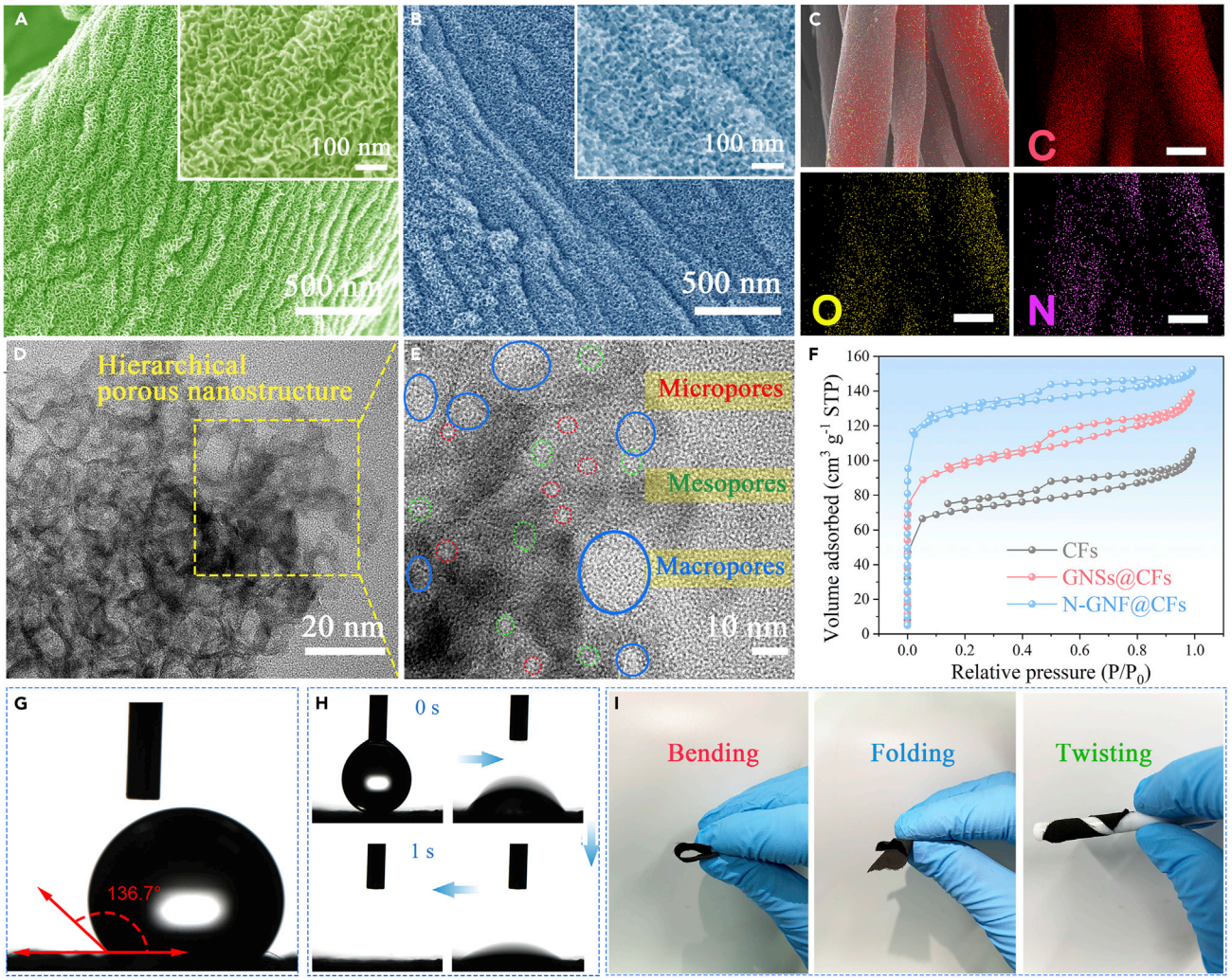

Figure 2. Microstructural characterizations and physical properties of materials

(A) SEM images of GNSs@CFs.

(B) SEM images of N-GNF@CFs.

(C) Element mappings of C, O, and N for N-GNF@CFs.

(D) TEM image of N-GNF@CFs.

(E) HR-TEM image of N-GNF@CFs.

(F) N_2 gas adsorption-desorption curves.

(G) Water contact angle of GNSs@CFs.

(H) Water contact angle of N-GNF@CFs.

(I) Flexibility of N-GNF@CFs electrode.

Microstructural and chemical characterizations of N-GNF@CFs electrode

The 3D hierarchical porous nanoarchitecture of N-GNF@CFs is initially examined by scanning electron microscopy (SEM). The SEM images of GNSs@CFs (Figure 2A) present a wrinkled surface from CFs. The larger magnification image (the inset of Figure 2A) identifies plentiful pure GNSs with well-architected distribution on the surface of CFs. It can be observed that the tortilla GNSs vertically and adjacently stack together to render a quasi-honeycomb structure encapsulating the CFs densely (Figure S2 and supplemental information), implying a high adhesion between the graphene and CFs. After N_2 plasma activation, these 2D GNSs arrays evolve into a coherent graphene nanofoam with a 3D interconnected porous network structure (Figure 2B), which is ascribed to the etching effect instigated by high-energy N_2 plasma, indicating that the graphene is successfully modified by the interaction of energetic electrons and active free radicals (N^{2+}/N^{+}) in the plasma system.[21,22] Note that plasma etching is distinguished from wet

chemical etching by the fact that it needs no liquids of corrosive acids or bases and long reaction time and the processing is highly reproducible and well-controlled.[23] To reveal the formation of such a delicate nanostructure of graphene, we also recorded the SEM images (Figure S3 and supplemental information) of the graphene at different N_2 plasma activation points in time. The structural characteristics transition of the graphene from nanosheet arrays to an integrated nanofoam with the increase of plasma treatment time is well presented in Figures S3A–S3C (supplemental information). However, the prolonged treatment leads to undesired structural damage to the graphene foam (Figure S3D and supplemental information), resulting in a significant reduction of the active layer, which is detrimental to the capacitive performance. Such 3D porous nanoarchitecture will effectively increase the surface area and expose more electrochemical active sites (i.e. doping N atoms), which is crucial to achieving enhanced capacitance and rate capability for carbon-based electrode materials.[24] The corresponding element mappings of N-GNF@CFs (Figure 2C) show that C, N, and O elements are homogeneously distributed, indicative of the doping of N atoms on graphene.

The nanoarchitecture of N-GNF@CFs is further demonstrated by a transmission electron microscope (TEM). Figure 2D displays the hierarchical porous structure with high interconnectivity of N-GNF@CFs, which guarantees more effective super high ways for fast electron migration.[25] The amplified region (Figure 2E) highlights these irregular and randomly distributed pores including micropores (<2 nm), mesopores (2-50 nm), and macropores (50-100 nm) throughout the substance, which is consistent with the SEM observation (Figure 2B). Given these observations, the N-GNF@CFs subjected to N_2 plasma activation would expose more surface area. Nitrogen adsorption-desorption measurements were conducted to further investigate the porosity characteristics of N-GNF@CFs. Figure 2F presents the N_2 adsorption-desorption isotherms of bare CFs, GNSs@CFs, and N-GNF@CFs, which exhibits a reversible type IV with a mesopore hysteresis loop at a relative pressure range of 0.45-0.9. The Brunauer-Emmett-Teller (BET) surface area of N-GNF@CFs (528 $m^2\ g^{-1}$) is much higher than that of pristine GNSs@CFs (417 $m^2\ g^{-1}$) and bare CFs (362 $m^2\ g^{-1}$), which is ascribed to the presence of more interconnected micro/mesopores induced by N_2 plasma activation. Moreover, the pore size distribution plots shown in Figure S4 (supplemental information) confirm the hierarchical porous structure of N-GNF@CFs, which is composed of abundant micropores and mesopores. The N_2 gas adsorption-desorption curves and the corresponding pore width distribution plots of N-GNF@CFs-5, N-GNF@CFs-10, and N-GNF@CFs-20 are presented in Figure S5 (supplemental information). The surface area of the initial N-GNF@CFs-5 is up to 477 $m^2\ g^{-1}$ by the contribution of micropores and mesopores. As the activation time extends to 10 min, the porous nanostructure enhanced significantly which results in a high surface area of 528 $m^2\ g^{-1}$. However, for a longer activation period of 20 min, micropores and mesopores decline and show an obvious diminution of surface area (367 $m^2\ g^{-1}$) closing to that of the bare CFs, confirming that the excessive N_2 plasma activation leads to the loss of the graphene on the surface of CFs, which is consistent with the results of SEM (Figure S3 and supplemental information).

The effect of the N_2 plasma activation on the wettability of graphene is also investigated since surface wettability is important to the transport rate of electrolyte ions at electrode/electrolyte interfaces. As shown in the water contact angle measurement results, the contact angle of the untreated GNSs@CFs is measured to be 136.7° (Figure 2G), whereas N-GNF@CFs exhibits super hydrophilicity with fast adsorption of a water droplet in 1s (Figure 2H). It is believed that the introduction of plenty of hydrophilic N-containing groups by N_2 plasma treatment is responsible for the improved wettability of N-CF@CFs. Besides, carbon fiber-based materials take advantage of flexibility and are lightweight in terms of applications in wearable and foldable SCs. As shown in Figure 2I, the free-standing N-GNF@CFs electrode exhibits good flexibility and practicability and can be bent, folded, and twisted freely, which is critical in the case of wearable and lightweight electronics.

To reveal more information about the crystalline structure and chemical composition of the graphene after N_2 plasma activation, X-ray diffraction (XRD), Raman, and (X-ray photoelectron spectroscopy) XPS were conducted. XRD pattern shows broad peaks at 24.0° and 43.7°, corresponding to the (002) and (100) planes of amorphous carbon from CFs (Figure 3A). Noticeably, the characteristic peaks of GNSs@CFs exhibit sharper than that of bare CFs indicating the graphite degree increased. Besides, a new sharp peak located at 26.2° for GNSs@CFs associated with (002) plane of graphite carbon (see the inset of Figure 3A), which confirms the successful synthesis of the GNSs on the surface of CFs.[26] After N_2 plasma activation, N-GNF@CFs shows a wider peak of the (002) plane at a lower diffraction angle, which is ascribed to the fact that abundant nitrogen atoms doping into the graphene increasing lattice spacing and generation

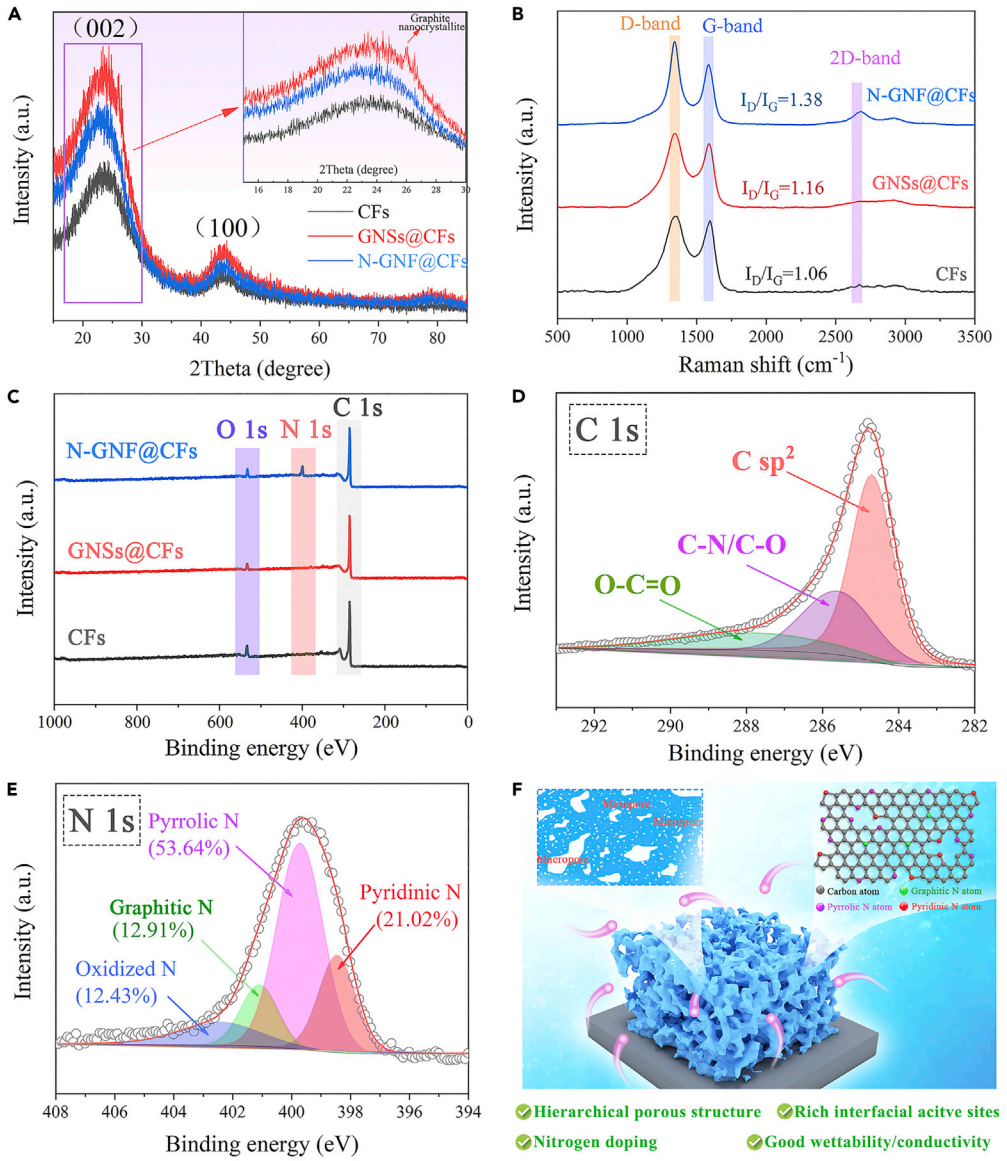

Figure 3. Chemical properties of the electrodes

(A) XRD patterns.

(B) Raman spectra.

(C) XPS survey spectra.

(D) High-resolution XPS spectra of N-GNF@CFs in the C 1s.

(E) High-resolution XPS spectra of N-GNF@CFs in the N 1s.

(F) The schematic illustration of the surface nanostructure of N-GNF@CFs, and its advantages as ideal electrode materials for SCs.

of more defects.[27] The Raman spectra in Figure 3B show a pronounce D band at 1350 cm^{-1} and a G band at 1596 cm^{-1}, corresponding to in-plane vibration of the graphite lattice and the feature of disordered graphite or crystal defects, respectively.[28] The intensity ratio of D and G bands (I_D/I_G) is widely used to determine the defect and graphitic degree of the carbon materials. The D to G peak intensity ratio (I_D/I_G) of the GNSs@CFs is estimated to be 1.16 which is larger than that of 1.06 for the pure CFs, suggesting the successful synthesis of graphene.[29] The I_D/I_G value of N-GNF@CFs increases to 1.38 indicating the greater disorder/defects, which can be attributed to the presence of N-containing functional groups on the surface of graphene together with dense reactive graphitic edges.[30]

X-ray photoelectron spectroscopy (XPS) is also used to identify the degree of doping N atoms. Figure 3C presents the typical XPS survey spectra with the characteristic peaks of C 1s and O1s, in which N-GNF@CFs exhibits a doping N 1s peak that can be quantified as the atomic ratio of 9.7%. The characteristic peak of C 1s spectrum located at 285.6 eV for N-GNF@CFs (Figure 3D) corresponds to the integrated contribution of C-O and C-N bond, in which the formation of C-N bond is ascribed to the N doping on the graphene after the N_2 plasma activation process. Moreover, the N 1s spectrum (Figure 3E) can be deconvoluted into four peaks, correlating to the pyridinic N (398.4 eV), pyrrolic N (399.7 eV), graphene N (401.1 eV), and oxidized N (402.4 eV) species, respectively.[31] The pyrrolic N is caused by the incorporation of N atoms into a five-membered heterocyclic ring, and pyridinic N is from the sp 2 hybridized N atom with two sp 2 hybridized C neighbors, while the graphitic N comes from sp 2 hybridized N atoms with three sp 2 hybridized C. It is reported that the doping N atoms on the edge of the graphite plane (pyrrolic N, pyridinic N, and oxidized N) can donate more effective active sites for the enhancement of catalytic and electrochemical performance compared with that of in the idle of the graphene plane (graphene N).[32] Notably, the percentage of N atoms on the edge of the graphite plane is 87.1%, much higher than in the middle of the graphite plane (12.9%), implying the existence of nitrogen at more effective active sites.

Based on the above characterization analysis, N-GNF@CFs, created using plasma activation technology, is expected to be an ideal free-standing electrode for high-performance SC in light of the advantages summarized in Figure 3F.

(1) The hierarchical porous nanostructure composed of well-distributed meso- and micropores significantly increases the specific surface area and may donate more extensive space for accepting adequate electrolyte solution to promote the charge propagation and ion transfer.

(2) Nitrogen doping induced by fast and facile N_2 plasma activation increases the conductivity of the material and exposes more active sites for electrochemical reactions, since the almost the nitrogen bonding configurations forming on the edge of graphene plane, which is expected to enhanced the capacitive of the electrode.

(3) The excellent wettability is conducive to improve the absorption of electrolyte and ionic conductivity, thus affecting the capacitance and cycling performance of the electrode.

Electrochemical properties of N-GNF@CFs electrode

The electrochemical properties of the N-GNF@CFs electrode were firstly assessed in a three-electrode system with the 3M KOH solution as electrolyte (Figure 4A). Figure 4B shows the cyclic voltammetry (CV) curves at 5 mV s^{-1} with a potential range of −1.0-0 V. Compared with GNSs@CFs and bare CFs, the CV trace of N-GNF@CFs displays an ideally quasi-rectangular features with an enlarged integral area, which confirms a considerably increased response current and enhanced capacitance of N-GNF@CFs. Notably, GNSs@CFs without any modification can exhibit a better electrochemical than CFs because the graphene possesses a larger surface area and higher electrical conductivity. Figure 4C shows the comparative galvanostatic charge-discharge (GCD) curves of N-GNF@CFs, GNSs@CFs, and CFs electrodes recorded at 1 mA cm^{-2}. The GCD curves of N-GNF@CFs shows a quasi-symmetric triangle, reflecting a high coulombic efficiency. Evidently, the disc harge time of the N-GNF@CFs is much longer than that of the GNSs@CFs and CFs electrodes, clearly revealing the increased capacitance of this electrode after the formation of 3D hierarchical porous nanostructure and functionalization with rich n-containing groups. Based on the discharge plots, the capacitance of the N-GNF@CFs is calculated to be 3.47 F cm^{-2} at 1 mA cm^{-2}, which is 2-fold greater than that of the untreated GNSs@CFs (1.61 F cm^{-2}) and is even 4-fold as much as that of CFs (1.01 F cm^{-2}) electrodes. Even at a large current density of 20 mA cm^{-2}, the N-GNF@CFs electrode still retains a high specific capacitance of 2.29 F cm^{-2} associating with high retention of 66%, indicatives of an impressive rate capability, whereas the specific capacitance of GNSs@CFs and CFs electrodes decrease to 0.80 F cm^{-2} (49.6%) and 0.19 F cm^{-2} (18.8%), respectively.

The Nyquist plots from electrochemical impedance spectroscopy (EIS) measurement in Figure 4E further reveal the reaction kinetics. The inset illustrates the fitted equivalent circuit composed of equivalent series resistance (Rs, composed of the intrinsic resistance, electrolyte ionic resistance, and interfacial resistance between the active materials and current collector), charge-transfer resistance (Rct), constant-phase element (CPE), and Warburg impedance (W). In the EIS curve, the value of Rs can be determined by the X-intercept in the high-frequency region and the diameter of the semicircle represents the values of Rct.

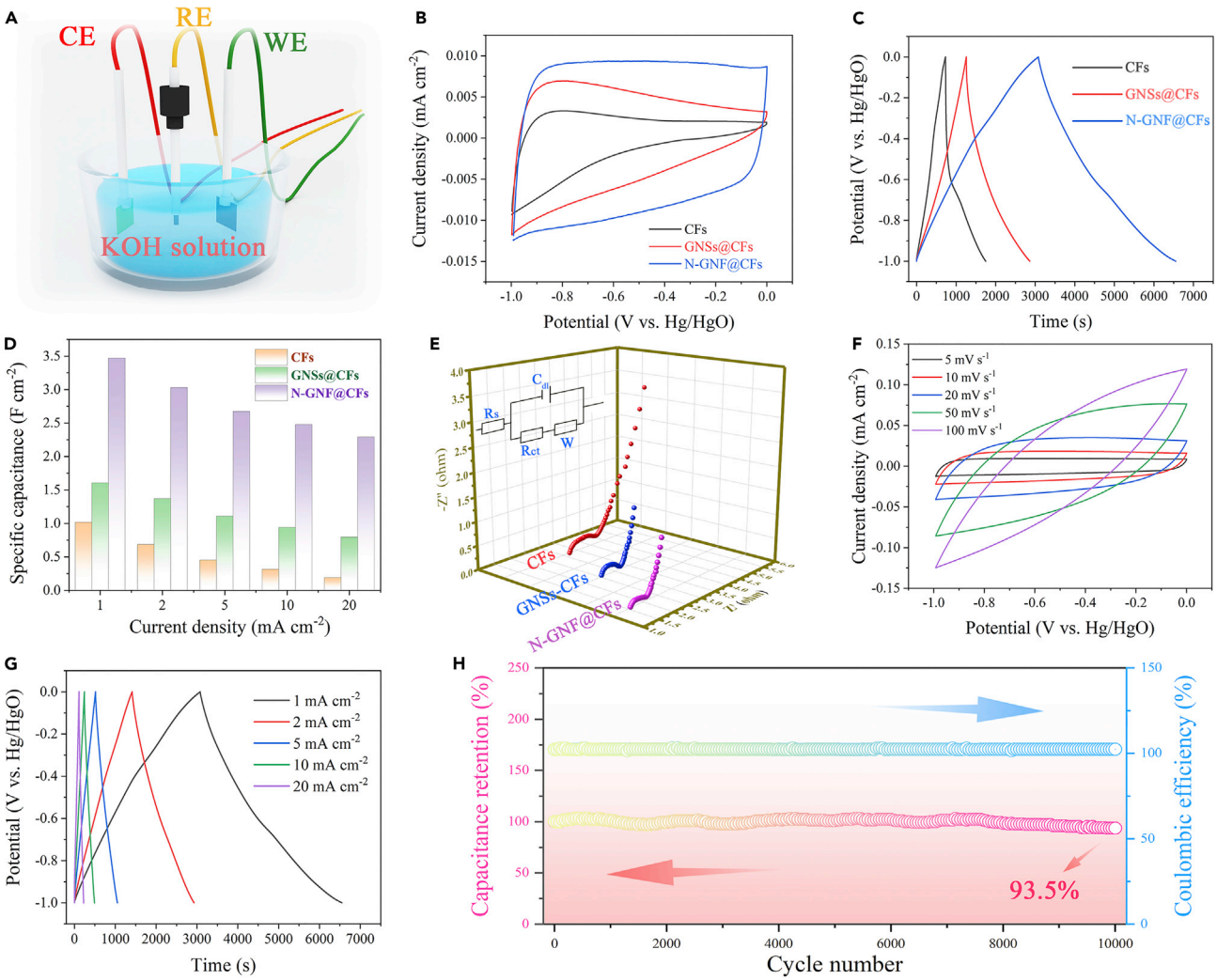

Figure 4. The electrochemical properties of the electrodes at three-electrodes system

(A) Schematic illustration of the three-electrode system.

(B) CV curves at 5 mV s^{-1}.

(C) GCD curves at 1 mA cm^{-2}.

(D) Area specific capacitance at different current densities.

(E) Nyquist plots (the inset refers to a fitting equivalent circuit).

(F) CV curves at various scan rates of N-GNF@CFs.

(G) GCD curves at the different current densities of N-GNF@CFs.

(H) Cyclic stability at 10 mA cm^{-2} for N-GNF@CFs.

In the low-frequency region, the slope of the curve is used to evaluate the W value, which is related to the ion diffusion at the electrode/electrolyte interface. The values of Rs and Rct of N-GNF@CFs are found to be 1.58 and 0.52 Ω, which are lower than that of GNSs@CF (2.53 and 0.72 Ω) and CFs (3.23 and 1.13 Ω), which demonstrates that the 3D hierarchical porous network nanostructure and doped electronegative nitrogen atoms dramatically improve the electrical conductivity and accelerate the charge transfer. Moreover, N-GNF@CFs also exhibits the highest slope which signifies a lower resistance of ion insertion/desertion and a superior capacitive property. These results are all well corresponding to CV and GCD results.

Considering the nanostructure of GNSs changes obviously with the prolongation of the N_2 plasma activation (Figure S3 and supplemental information), we further study the effect of plasma treatment time on the electrode electrochemical properties. The comparison of CV and GCD curves of the various electrodes obtained after 0 min (GNSs@CFs), 5min (N-GNF@CFs-5), 10 min (N-GNF@CFs-10), and 20 min (N-GNF@CFs-20) N_2

plasma treatment is shown in Figure S6 (supplemental information). It is manifest that the integrating areas of the CV curves (Figure S6A and supplemental information) expand gradually with the increase of activation time from initial 0 to 10 min, indicating that the N_2 plasma activation exposes more active sites to the surface of graphene and increases the surface area, thus improves the charge storage capability. Unfortunately, the immoderate treatment time results in an undesirable degeneration of electrochemical properties of N-GNF@CFs-20, which is because the excessive etching derived from the active reaction between gas ions and the active layer almost eliminates the active substance from the surface of CFs (Figure S3D and supplemental information). Thereupon, the N-GNF@CFs-10 with hierarchical porous structure is determined as the optimized subject and is represented by N-GNF@CFs in this article. The detailed electrochemical properties of GNSs@CFs, N-GNF@CFs-5, and N-GNF@CFs-20 are shown in Figure S7 (supplemental information). The CV curves of N-GNF@CFs at various scan rates are shown in Figure 4F. Apparently, the shape of the curves is well maintained, even at a high scan rate of 100 mV s^{-1}, demonstrating a good rate capability and fast electron transfer in the electrode. Figure 4G presents the GCD curves of N-GNF@CFs at different current densities. The GCD curves are a nearly symmetrical triangle and agreed well with the results of CV analysis, indicating typical double-layer capacitance characteristics with a high coulombic efficiency (~98%). Moreover, the N-GNF@CFs exhibits excellent cycling stability over 10,000 GCD cycles by maintaining 96.4% of its initial capacitance (Figure 4H), indicative of appropriateness for long-life energy storage devices.

Electrochemical properties of N-GNF@CFs electrode based flexible zinc ion capacitor device

Based on the above analysis, we believe that N-GNF@CFs is qualified to be an ideal electrode for high-performance SCs devices. Zn ion capacitor (ZIC) is a promising novel hybrid energy storage device that stores energy through reversible anion adsorption/desorption onto the SC-type carbon cathode and reversible Zn ions (as charge carriers) deposition/extraction onto the battery-type Zn anode.[33] Herein, Zn anode which is composed of Zn nanosheets and CFs (Zn NSs@CFs) was fabricated by one-step electrodeposition.[34] Specifically, A three-electrode system was used for electrochemical deposition, where CFs substrate, platinum plate and saturated calomel electrode were taken as working, counter and reference electrodes respectively, and 100 mL mixed solution of $ZnSO_4$, Na_2SO_4 and boric acid as the electrolyte. The synthesis process was carried out at a constant current of 60 mA for 15 min. The growth mechanism of electrodeposited Zn NSs is composed three plausible processes as illustrated in Figure S8A.[35,36] At the beginning, plenty of Zn^{2+} in the electrolyte solution were adsorbed to the surface of CFs for a cathodic reaction, i.e. reducing Zn^{2+} to Zn metal. Subsequently, a layer of Zn film was firstly formed and encapsulated onto the CFs. As the reaction progress, the nucleation and crystallization begin, in which a few of Zn nanosheets sprouted from the thin layer of the Zn film. Afterward, all the Zn film served as a seed layer for the aggregative growth of nanosheets. With the deposition time gradually prolonged, more and more Zn NSs formed.

SEM images (Figure S8B) confirm that numerous Zn NSs were homogeneously deposited onto the surface of CFs. The high-magnification SEM image further displays the vertically interconnected nanosheets with diameter of 1.5-2 μm. It is believed that such well distributed nanosheet arrays without aggregation can significantly reduce the intrinsic resistance for fast electron transfer and provide favorable pathway for deposition/extraction process of Zn/Zn^{2+}.[34] The corresponding elemental mapping images (Figures S8C-S8E) and EDX spectrum (Figure S8F) also verify the uniform distribution of Zn elements on the surface of CFs. The XRD pattern of Zn NSs@CFs (Figure S8G) displays the characteristic peaks at 36.4°, 39.0°, 43.3°, 54.4°, 70.1°, and 70.7°, which correspond well to the (002), (100), (101), (102), (103) and (110) planes of hexagonal zinc (JCPDS: 87-0713), respectively.[37] A broad and indistinctive peak at ~24° refers to the (002) plane of amorphous carbon, suggesting the Zn NSs tend to congregate toward the high-density distribution. No excrescent peaks are observed, indicating the high purity and good crystallinity of the as-prepared Zn metal.

We used N-GNF@CFs as cathode, Zn NSs@CFs as anode, and 1 M $ZnSO_4$/gelatin as gel electrolyte to constructed the flexible quasi-solid-state ZIC (i.e. N-GNF@CFs//Zn NSs@CFs, abbreviated as N-GNF@CFs ZIC), which assembled structure illustration is shown in Figure 5A. Figure 5B schematically depicts the charge storage mechanism of the N-GNF@CFs ZIC. During charging, the SO_4^{2-} ions are adsorbed onto the surface of the N-GNF@CFs, while the Zn^{2+} ions in the electrolyte are deposited onto the Zn NSs@CFs. During discharge, SO_4^{2-} ions leave the surface of the N-GNF@CFs electrode and back to the electrolyte, while Zn^{2+} ions are extracted from the Zn NSs@CFs. The electrochemical properties of the ZICs were comprehensively studied using CV and GCD measurements. Figure 5C shows the comparative

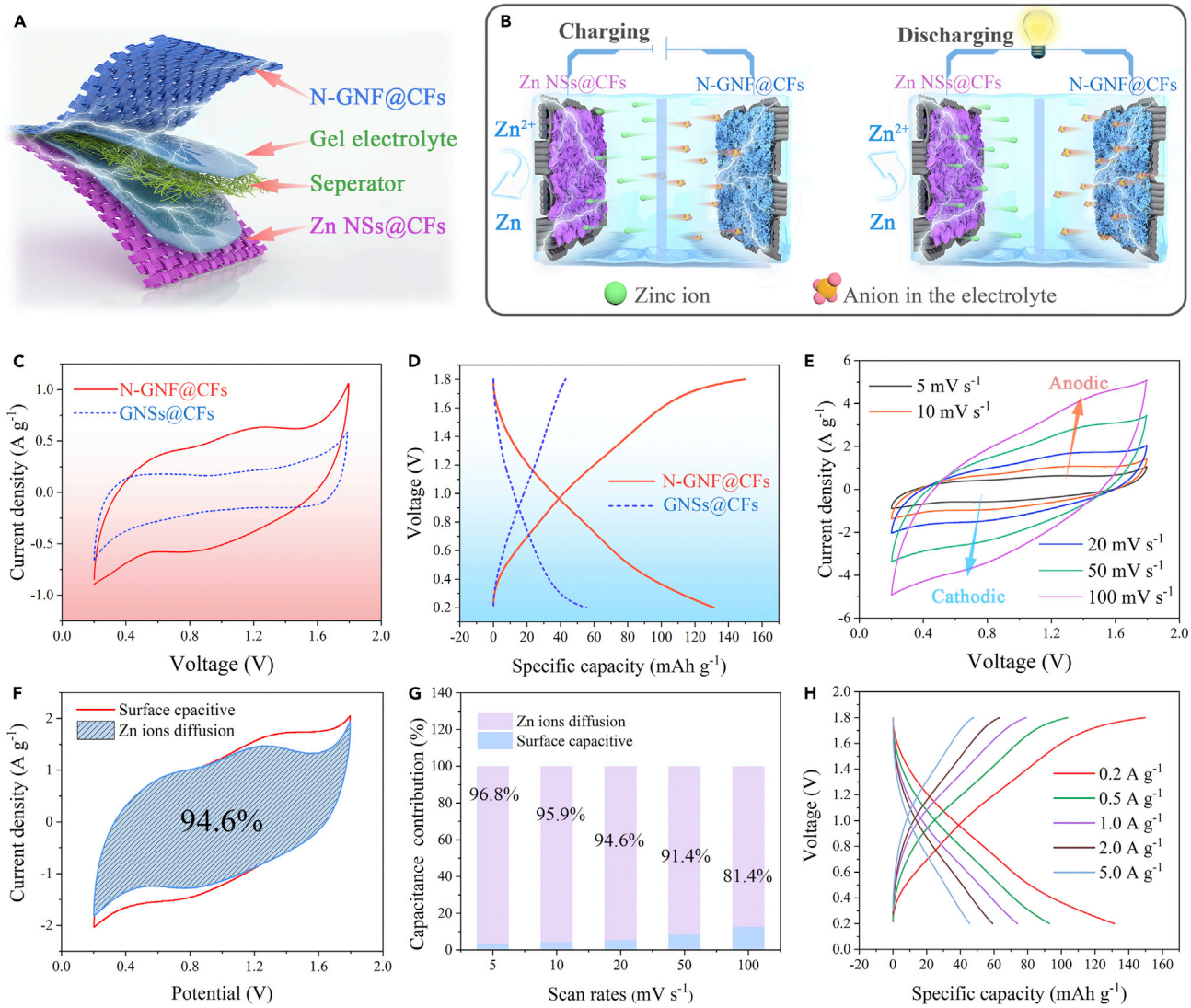

Figure 5. Electrochemical performances of flexible ZIC devices

(A) The schematic illustration of the structure of flexible quasi-solid-state ZIC.

(B) The charge storage mechanism of ZIC.

(C) CV curves at 5 mV s^{-1}.

(D) GCD curves at 0.2 A g^{-1}.

(E) CV curves of N-GNF@CFs ZIC at various scan rates.

(F) Fitting result of the contribution of Zn ions diffusion based on the CV curve at 20 mV s^{-1} for N-GNF@CFs ZIC.

(G) Histogram illustration of the contribution ratio of the capacitive capacities and Zn ions diffusion at different scan rates.

(H) GCD curves at various current densities of N-GNF@CFs ZIC.

CV curves of N-GNF@CFs and GNSs@CFs ZICs at a scan rate of 5 mV s^{-1} in the voltage window from 0.2 to 1.8 V. As is shown, both the CV curves exhibit a non-ideal rectangle shape, and no obvious oxygen and hydrogen evolution peaks occur, indicating the different charge storage mechanisms of the carbon cathode (i.e. reversible SO_4^{2-} adsorption/desorption) and Zn anode (i.e. Zn^{2+} deposition/stripping) in a ZIC working in a stable voltage.[38] The integrated area of the CV curves for N-GNF@CFs ZIC is much larger than that of GNSs@CFs based ZIC, indicative of the larger capacity of N-GNF@CFs ZIC. The GCD curves of N-GNF@CFs and GNSs@CFs ZICs at the current density of 0.2 A g^{-1} exhibit the discharge specific capacities of 131.5 and 54.4 mAh g^{-1} (263 and 108.8 F g^{-1}) (Figure 5D). Notably, the discharge capacity of N-GNF@CFs is higher than the charge capacity because of the incomplete adsorption/desorption of Zn^{2+} onto the surface of electrode in the initial cycles. As to the detailed CV curves of N-GNF@CFs and

GNSs@CFs ZICs shown in Figure 5E and Figure S9A (supplemental information), all the curves display similarly shaped even at a high scan rate of 100 mV s^{-1}. Specifically, a pair of weak peaks appear at cathodic (0.8 V) and anodic (1.3 V) sweeps for N-GNF@CFs ZIC, suggesting the existence of a reversible Faradic redox reaction, thus endowing the configuration with extra capacity abilities stemming from pseudocapacitance. Such synergistically pseudocapacitive behavior is ascribed to the N-containing groups on the surface of this carbon material, which is treated by the fast and facile N_2 plasma activation.

We further revealed the energy storage mechanism of the N-GNF@CFs ZIC and the electrochemical kinetic analysis was performed by using Dunn's method.[39] Based on the CV curves, the power-law relationship between peak current (i) and scan rate (v) can be expressed as Equations 1 and 2:

$$i = a \times v^b \quad \text{(Equation 1)}$$

$$\log(i) = b \log(v) + \log(a) \quad \text{(Equation 2)}$$

Where a and b are alterable parameters. Typically, the value of b is 0.5 represents a ions diffusion-controlled electrochemical behavior, while b = 1.0 indicates a surface capacitive process. As shown in Figure S10 (supplemental information), the value of b is calculated to be 0.63 and 0.61 corresponding to anodic and cathodic currents respectively, confirming that the combined behavior of ion diffusion and capacitive co-controls the charge storage process, in which the Zn ion diffusion-controlled process dominates the electrochemical behavior.[40] The capacitive and diffusion-controlled contributions can be further quantitatively examined by using Equation 3:

$$i(V) = k_1 v + k_2 v^{1/2} \quad \text{(Equation 3)}$$

In which $k_1 v$ refers to the capacitive current part and $k_1 v^{1/2}$ is the diffusion-controlled current part. The values of k_1 and k_2 can be determined by plotting $i/v^{1/2}$ vs. $k_1 v^{1/2}$ at various potentials and scan rates according to the converted Equation 4:

$$i(V) / v^{1/2} = k_1 v^{1/2} + k_2 \quad \text{(Equation 4)}$$

Figure 5F shows the CV curves at 20 mV s^{-1} of N-GNF@CFs, in which the fraction of Zn ions diffusion-controlled contribution (blue area) to the total current is calculated as 94.6%. The rate of diffusion-controlled contribution at various scan rates is also calculated and the results are shown in Figure 5G. As is shown, the contribution of the diffusion-controlled process decreases from 96.8% to 81.4% as the scan rate increases from 5 to 100 mV s^{-1}, while the capacitive contribution increases gradually. These results help to elucidate the typical battery-type characteristic of the N-GNF@CFs based ZIC, which performs charge storage through reversible adsorption/desorption of Zn ions. What's more, the abundant nitrogen-containing functional groups increase the active sites and 3D hierarchical porous nanostructure enlarges the surface area, thus providing more opportunity for a pseudocapacitive reaction.

The GCD curves at different current densities of the N-GNF@CFs and GNSs@CFs based ZICs are displayed in Figures 5H and S9B (supplemental information). According to the discharge curves, the capacity of N-GNF@CFs ZIC at 0.2 A g^{-1} shows a high value of 131.5 mAh g^{-1} (263 F g^{-1}), which is higher than twice that of GNSs@CFs ZIC (54.4 mAh g^{-1}, i.e. 108.8 F g^{-1}). The values of capacity at various current densities for the ZICs are shown in Figure S11 (supplemental information) and Figure 6A. Notably, N-GNF@CFs ZIC can exhibit the capacity of 45.5 mAh g^{-1} (91 F g^{-1}) even when the high current density increases up to 5.0 A g^{-1}, while GNSs@CFs ZIC fails to sustain such a large current density and only shows a capacity of 14.1 mAh g^{-1} (28.2 F g^{-1}) at 2.0 A g^{-1}, which suggests the excellent rate capability of N-GNF@CFs. Furthermore, the cyclic test of N-GNF@CFs ZIC was conducted and the result is also recorded in Figure 6A. After an ultra-long 10,000 GCD cycles at a current density of 2.0 A g^{-1}, the capacity retention of this quasi-solid-state ZIC is as high as 87.9%, indicative of excellent cycle stability. Owing to the remarkable capacity and relatively wide voltage window, the N-GNF@CFs ZIC device achieves high energy and power densities up to 105.2 Wh kg^{-1} at 378.6 W kg^{-1}. Even at a high power density of 11,250 W kg^{-1}, the energy density remains to 36.4 Wh kg^{-1}. Seeing from the Ragone plot in Figure 6B, these values can bear comparison with the typical ZIC device of NOCS//Zn (109.5 Wh kg^{-1}, 225.0 W kg^{-1}),[41] even outperform those of MnO_2-CNT//$Ti_3C_2T_x$ (67.8 Wh kg^{-1}, 59.9 W kg^{-1}),[42] PDC//Zn foil (48.0 Wh kg^{-1}, 85.0 W kg^{-1}),[43] OPC/CC//Zn/CC (82.4 Wh kg^{-1}, 44.1 W kg^{-1}),[34] rGO-NbPO//Zn-foil (56.0 Wh kg^{-1} , 1000.0 W kg^{-1})[44] and UPCSs//Zn foil (75.2 Wh kg^{-1}, 36.6 W kg^{-1}).[45] More detailed information is available in Table S1 and supplemental information. The

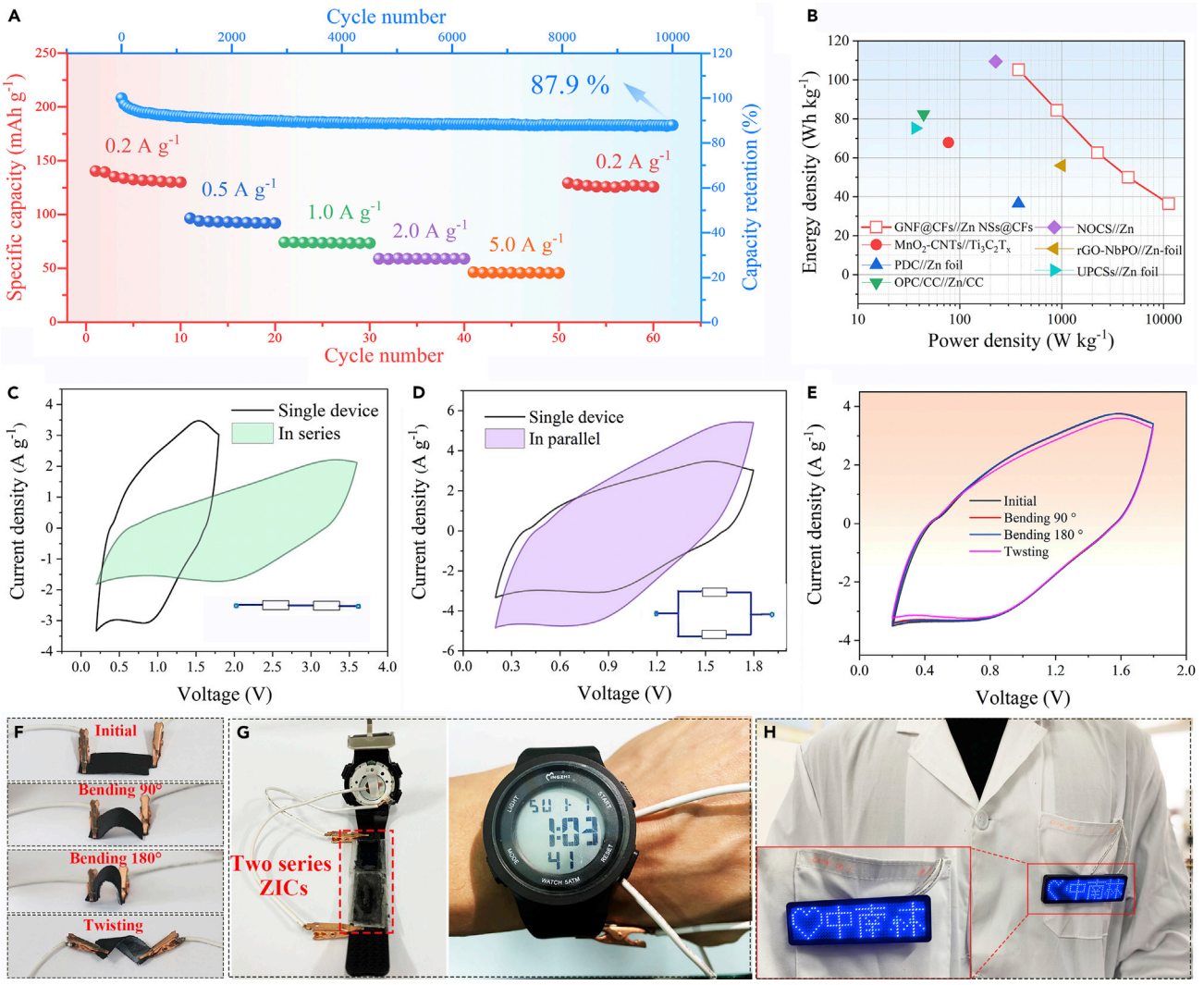

Figure 6. Electrochemical performances of N-GNF@CFs ZIC device and its applications in wearable electronics

(A) Rate capability at various rates and cycling stability at the current density of 5.0 A g^{-1}.

(B) Ragon plots.

(C) CV curves of a single ZIC device.

(D) Two devices connected in series or in parallel.

(E) CV curves at 50 mV s^{-1}.

(F) The flexible ZIC devices at different bending and twisting conditions.

(G) Powering a sport watch.

(H) Lamping a Mini LED panel.

above results exhaustively demonstrate the excellent electrochemical performance of the flexible N-GNF@CFs based ZIC.

Compared with metal-based energy storage devices, carbon fiber-based energy storage devices have advantages of lightweight, excellent flexibility, and easy to customize sizes. The most important thing is that CFs are able to prevent the exfoliation of the superficial active substance during harsh deformations under external forces due to its rough surfaces and the strong intermolecular bonds between subject and guest substances. Besides, multiple flexible devices may be connected in series or in parallel to create integrated power supply with extensive output voltage and current to fulfill the different power and energy requirements. In consideration of these intriguing advantages, we further assessed the feasibility of the flexible N-GNF@CFs quasi-solid-state ZIC in practical applications. Figures 6C and 6D depict the compared CV profiles of a single device, two devices

connected in series and in parallels measured at a sweep rate of 50 mV s^{-1}. As is shown, the working voltage window is increased from 1.8 V for single device to 3.6 V for two devices in series connection without the shape distortion of CV curve, while two devices in parallels connection show an almost twice large response current than that of single device at the same voltage of 1.8 V. Moreover, as a flexible device, N-GNF@CFs ZIC can be bent and twisted without structural failure and electrolyte leakage (Figure 6F) which is benefited from the mechanical stability of flexible carbon fiber-based electrodes and gelatin gel electrolyte. The corresponding CV curves at 50 mV s^{-1} of the ZIC with different bending angles (0°, 90°, 180°) and twisting state remain similar shapes compared to the original state (Figure 6E), verifying the excellent capability of deformation resistance. Finally, we successfully powered the electric swatch (Figure 6G) and Mini LED plane (Figure 6H) by using the as-fabricated quasi-solid-state N-GNF@CFs ZICs.

DISCUSSION

In summary, a novel N-doped and 3D hierarchical porous freestanding electrode materials with outstanding SC performance has been demonstrated by employing a facile, fast and eco-friendly strategy of combining Ar/CH_4 plasma deposition and N_2 plasma activation. The advanced N-GNF@CFs favors fast ion/electron transport and ensures sufficient space for charge storage, which benefits by integrated merits of the interconnected porous nanofoam architecture with abundant micro- and mesopores, large specific surface area and excellent hydrophilicity. The electrochemical investigation showed that the N-GNF@CFs delivered a high discharge-specific capacity of 204.2 F g^{-1} at a current density of 1 mA cm^{-2}. Moreover, the as-designed electrodes presented excellent rate performance and high cyclic stability. What's more, the as-prepared flexible quasi-solid-state N-GNF@CFs//Zn NSs@CFs ZIC exhibits ultra-high energy density of 105.2 Wh kg^{-1} at 378.6 W kg^{-1}, and long-term cycling stability (~87.9% capacitance retention after 10,000 cycles). This study provides an illuminating insight for the development of nanostructured electrode materials their application in the next generation of green and efficient energy storage devices.

Limitations of the study

The 3D nanostructure of N-GNF@CFs is comprised of rich micro- and mesopores, which is crucial for ion transportation and charge storage. However, there are lack of more precise and quantitative characterizations to reveal the ion transfer property in this porous nanostructure. Moreover, such unique nanoarchitecture shows potential to act as the 3D framework for introducing and stabilizing the guest active materials with high theoretic capacitance, which is one of our interests focusing on developing novel high performance electrode materials for energy storage.

STAR★METHODS

Detailed methods are provided in the online version of this paper and include the following:

- KEY RESOURCES TABLE
- RESOURCE AVAILABILITY
  - Lead contact
  - Materials availability
  - Data and code availability
- METHOD DETAILS
  - Preparation of CFs
  - Preparation of GNSs@CFs and N–GNF@CFs
  - Preparation of the flexible quasi-solid-state ZIC
  - Material characterizations
  - Electrochemical characterizations
  - Calculations
- QUANTIFICATION AND STATISTICAL ANALYSIS

SUPPLEMENTAL INFORMATION

Supplemental information can be found online at https://doi.org/10.1016/j.isci.2023.105964.

ACKNOWLEDGMENTS

This study was supported by the National Natural Science Foundation of China (grant nos. 31890771 and 31901249), Hunan Provincial Technical Innovation Platform and Talent Program in Science and Technology

(grant no. 2020RC3041), Hunan Provincial Innovation Foundation for Postgraduate (grant no. CX20210842), Training Program for Excellent Young Innovators of Changsha (grant no. kq2106056), and Hunan Provincial Natural Science Foundation of China (grant no. 2022JJ30079).

AUTHOR CONTRIBUTIONS

Conceptualization, Y.W. and S.W.; methodology, C.W.; formal analysis, S.W.; investigation, S.J. and C.W.; resources, H.C.; writing – original draft, S.W.; writing – review & editing, Y.W. and C.W.; visualization: S.W. and C.W.; supervision, X.L. funding acquisition, Y.W., C.W., and S.W..

DECLARATION OF INTERESTS

The authors declare no competing interests.

INCLUSION AND DIVERSITY

While citing references scientifically relevant for this work, we also actively worked to promote gender balance in our reference list.

Received: May 25, 2022
Revised: November 22, 2022
Accepted: January 6, 2023
Published: January 13, 2023

REFERENCES

1. Raza, W., Ali, F., Raza, N., Luo, Y., Kim, K.-H., Yang, J., Kumar, S., Mehmood, A., and Kwon, E.E. (2018). Recent advancements in supercapacitor technology. Nano Energy *52*, 441–473. https://doi.org/10.1016/j.nanoen.2018.08.013.

2. Yu, Z., Tetard, L., Zhai, L., and Thomas, J. (2015). Supercapacitor electrode materials: nanostructures from 0 to 3 dimensions. Energy Environ. Sci. *8*, 702–730. https://doi.org/10.1039/c4ee03229b.

3. Yang, Y. (2020). A mini-review: emerging all-solid-state energy storage electrode materials for flexible devices. Nanoscale *12*, 3560–3573. https://doi.org/10.1039/c9nr08722b.

4. Wang, H., Ye, W., Yang, Y., Zhong, Y., and Hu, Y. (2021). Zn-ion hybrid supercapacitors: achievements, challenges and future perspectives. Nano Energy *85*, 105942. https://doi.org/10.1016/j.nanoen.2021.105942.

5. Frackowiak, E. (2007). Carbon materials for supercapacitor application. Phys. Chem. Chem. Phys. *9*, 1774–1785. https://doi.org/10.1039/b618139m.

6. Zhou, Y., Jia, Z., Shi, L., Wu, Z., Jie, B., Zhao, S., Wei, L., Zhou, A., Zhu, J., Wang, X., and Fu, Y. (2020). Pressure difference-induced synthesis of P-doped carbon nanobowls for high-performance supercapacitors. Chem. Eng. J. *385*, 123858. https://doi.org/10.1016/j.cej.2019.123858.

7. Liang, J., Qu, T., Kun, X., Zhang, Y., Chen, S., Cao, Y.-C., Xie, M., and Guo, X. (2018). Microwave assisted synthesis of camellia oleifera shell-derived porous carbon with rich oxygen functionalities and superior supercapacitor performance. Appl. Surf. Sci. *436*, 934–940. https://doi.org/10.1016/j.apsusc.2017.12.142.

8. Wei, W., Chen, Z., Zhang, Y., Chen, J., Wan, L., Du, C., Xie, M., and Guo, X. (2020). Full-faradaic-active nitrogen species doping enables high-energy-density carbon-based supercapacitor. J. Energy Chem. *48*, 277–284. https://doi.org/10.1016/j.jechem.2020.02.011.

9. Zhang, S., Yu, Y., Xie, M., Du, C., Chen, J., Wan, L., and Zhang, Y. (2022). Clean production of N, O-doped activated carbon by water vapor carbonization/activation of expired coffee for high-volumetric supercapacitor. Appl. Surf. Sci. *589*, 153011. https://doi.org/10.1016/j.apsusc.2022.153011.

10. Fan, H., Mao, K., Liu, M., Zhuo, O., Zhao, J., Sun, T., Jiang, Y., Du, X., Zhang, X., Wu, Q., et al. (2018). Tailoring the nano heterointerface of hematite/magnetite on hierarchical nitrogen-doped carbon nanocages for superb oxygen reduction. J. Mater. Chem. *6*, 21313–21319. https://doi.org/10.1039/c8ta06442c.

11. Xu, F., Zhai, Y., Zhang, E., Liu, Q., Jiang, G., Xu, X., Qiu, Y., Liu, X., Wang, H., and Kaskel, S. (2020). Ultrastable surface-dominated pseudocapacitive potassium storage enabled by edge-enriched N-doped porous carbon nanosheets. Angew. Chem. Int. Ed. Engl. *132*, 19628–19635. https://doi.org/10.1002/ange.202005118.

12. Wang, C., Wang, F., Liu, Z., Zhao, Y., Liu, Y., Yue, Q., Zhu, H., Deng, Y., Wu, Y., and Zhao, D. (2017). N-doped carbon hollow microspheres for metal-free quasi-solid-state full sodium-ion capacitors. Nano Energy *41*, 674–680. https://doi.org/10.1016/j.nanoen.2017.10.025.

13. Zhang, Y., Rawat, R.S., and Fan, H.J. (2017). Plasma for rapid conversion reactions and surface modification of electrode materials. Small Methods *1*, 1700164. https://doi.org/10.1002/smtd.201700164.

14. Ouyang, B., Zhang, Y., Wang, Y., Zhang, Z., Fan, H.J., and Rawat, R.S. (2016). Plasma surface functionalization induces nanostructuring and nitrogen-doping in carbon cloth with enhanced energy storage performance. J. Mater. Chem. *4*, 17801–17808. https://doi.org/10.1039/c6ta08155j.

15. Jeong, H.M., Lee, J.W., Shin, W.H., Choi, Y.J., Shin, H.J., Kang, J.K., and Choi, J.W. (2011). Nitrogen-doped graphene for high-performance ultracapacitors and the importance of nitrogen-doped sites at basal planes. Nano Lett. *11*, 2472–2477. https://doi.org/10.1021/nl2009058.

16. Singh, G., Sutar, D.S., Divakar Botcha, V., Narayanam, P.K., Talwar, S.S., Srinivasa, R.S., and Major, S.S. (2013). Study of simultaneous reduction and nitrogen doping of graphene oxide Langmuir-Blodgett monolayer sheets by ammonia plasma treatment. Nanotechnology *24*, 355704. https://doi.org/10.1088/0957-4484/24/35/355704.

17. Ouyang, B., Zhang, Y., Xia, X., Rawat, R.S., and Fan, H.J. (2018). A brief review on plasma for synthesis and processing of electrode materials. Mater. Today Nano *3*, 28–47. https://doi.org/10.1016/j.mtnano.2018.11.002.

18. Wei, S., Wan, C., Zhang, L., Liu, X., Tian, W., Su, J., Cheng, W., and Wu, Y. (2022). N-doped and oxygen vacancy-rich NiCo2O4 nanograss for supercapacitor electrode. Chem. Eng. J. *429*, 132242. https://doi.org/10.1016/j.cej.2021.132242.

19. Wei, S., Wan, C., Jiao, Y., Li, X., Li, J., and Wu, Y. (2020). 3D nanoflower-like MoSe2 encapsulated with hierarchically anisotropic carbon architecture: a new and free-standing anode with ultra-high areal capacitance for asymmetric supercapacitors. Chem. Commun. *56*, 340–343. https://doi.org/10.1039/c9cc07362k.

20. Imran Jafri, R., Rajalakshmi, N., and Ramaprabhu, S. (2010). Nitrogen doped graphene nanoplatelets as catalyst support for oxygen reduction reaction in proton exchange membrane fuel cell. J. Mater. Chem. *20*, 7114. https://doi.org/10.1039/c0jm00467g.

21. Xu, L., Jiang, Q., Xiao, Z., Li, X., Huo, J., Wang, S., and Dai, L. (2016). Plasma-engraved Co3 O4 nanosheets with oxygen vacancies and high surface area for the oxygen evolution reaction. Angew. Chem. Int. Ed. Engl. *55*, 5277–5281. https://doi.org/10.1002/anie.201600687.

22. Adhamash, E., Pathak, R., Chen, K., Rahman, M.T., El-Magrous, A., Gu, Z., Lu, S., Qiao, Q., and Zhou, Y. (2020). High-energy plasma activation of renewable carbon for enhanced capacitive performance of supercapacitor electrode. Electrochim. Acta *362*, 137148. https://doi.org/10.1016/j.electacta.2020.137148.

23. Liang, H., Ming, F., and Alshareef, H.N. (2018). Applications of plasma in energy conversion and storage materials. Adv. Energy Mater. *8*, 1801804. https://doi.org/10.1002/aenm.201801804.

24. Shang, Z., An, X., Zhang, H., Shen, M., Baker, F., Liu, Y., Liu, L., Yang, J., Cao, H., Xu, Q., et al. (2020). Houttuynia-derived nitrogen-doped hierarchically porous carbon for high-performance supercapacitor. Carbon *161*, 62–70. https://doi.org/10.1016/j.carbon.2020.01.020.

25. Tian, Z.-F., Xie, M.-J., Shen, Y., Wang, Y.-Z., and Guo, X.-F. (2017). Fabrication of sulfonated mesoporous carbon by evaporation induced self-assembly/carbonization approach and its supercapacitive properties. Chin. Chem. Lett. *28*, 863–867. https://doi.org/10.1016/j.cclet.2016.12.004.

26. Cai, J., Wu, C., Yang, S., Zhu, Y., Shen, P.K., and Zhang, K. (2017). Templated and catalytic fabrication of N-doped hierarchical porous carbon-carbon nanotube hybrids as host for lithium-sulfur batteries. ACS Appl. Mater. Interfaces *9*, 33876–33886. https://doi.org/10.1021/acsami.7b09808.

27. Geng, D., Yang, S., Zhang, Y., Yang, J., Liu, J., Li, R., Sham, T.-K., Sun, X., Ye, S., and Knights, S. (2011). Nitrogen doping effects on the structure of graphene. Appl. Surf. Sci. *257*, 9193–9198. https://doi.org/10.1016/j.apsusc.2011.05.131.

28. Zhang, Z., Li, W., Yuen, M.F., Ng, T.-W., Tang, Y., Lee, C.-S., Chen, X., and Zhang, W. (2015). Hierarchical composite structure of few-layers MoS 2 nanosheets supported by vertical graphene on carbon cloth for high-performance hydrogen evolution reaction. Nano Energy *18*, 196–204. https://doi.org/10.1016/j.nanoen.2015.10.014.

29. Yang, C., Bi, H., Wan, D., Huang, F., Xie, X., and Jiang, M. (2013). Direct PECVD growth of vertically erected graphene walls on dielectric substrates as excellent multifunctional electrodes. J. Mater. Chem. *1*, 770–775. https://doi.org/10.1039/c2ta00234e.

30. Ito, Y., Qiu, H.J., Fujita, T., Tanabe, Y., Tanigaki, K., and Chen, M. (2014). Bicontinuous nanoporous N-doped graphene for the oxygen reduction reaction. Adv. Mater. *26*, 4145–4150. https://doi.org/10.1002/adma.201400570.

31. Mou, X., Ma, J., Zheng, S., Chen, X., Krumeich, F., Hauert, R., Lin, R., Wu, Z., and Ding, Y. (2020). A general synthetic strategy toward highly doped pyridinic nitrogen-rich carbons. Adv. funct. Mater. *31*, 2006076. https://doi.org/10.1002/adfm.202006076.

32. Guo, D., Shibuya, R., Akiba, C., Saji, S., Kondo, T., and Nakamura, J. (2016). Active sites of nitrogen-doped carbon materials for oxygen reduction reaction clarified using model catalysts. Science *351*, 361–365. https://doi.org/10.1126/science.aad0832.

33. Shao, Y., Sun, Z., Tian, Z., Li, S., Wu, G., Wang, M., Tong, X., Shen, F., Xia, Z., Tung, V., et al. (2020). Regulating oxygen substituents with optimized redox activity in chemically reduced graphene oxide for aqueous Zn-ion hybrid capacitor. Adv. funct. Mater. *31*, 2007843. https://doi.org/10.1002/adfm.202007843.

34. Zheng, Y., Zhao, W., Jia, D., Liu, Y., Cui, L., Wei, D., Zheng, R., and Liu, J. (2020). Porous carbon prepared via combustion and acid treatment as flexible zinc-ion capacitor electrode material. Chem. Eng. J. *387*, 124161. https://doi.org/10.1016/j.cej.2020.124161.

35. Zhang, P., Li, Y., Wang, G., Wang, F., Yang, S., Zhu, F., Zhuang, X., Schmidt, O.G., and Feng, X. (2019). Zn-ion hybrid micro-supercapacitors with ultrahigh areal energy density and long-term durability. Adv. Mater. *31*, e1806005. https://doi.org/10.1002/adma.201806005.

36. Yang, J., Wang, Y., Kong, J., Jia, H., and Wang, Z. (2015). Synthesis of ZnO nanosheets via electrodeposition method and their optical properties, growth mechanism. Opt. Mater. *46*, 179–185. https://doi.org/10.1016/j.optmat.2015.04.016.

37. Zeng, Y., Zhang, X., Meng, Y., Yu, M., Yi, J., Wu, Y., Lu, X., and Tong, Y. (2017). Achieving ultrahigh energy density and long durability in a flexible rechargeable quasi-solid-state Zn-MnO2 battery. Adv. Mater. *29*, 1700274. https://doi.org/10.1002/adma.201700274.

38. Hao, J., Li, B., Li, X., Zeng, X., Zhang, S., Yang, F., Liu, S., Li, D., Wu, C., and Guo, Z. (2020). An in-depth study of Zn metal surface chemistry for advanced aqueous Zn-ion batteries. Adv. Mater. *32*, e2003021. https://doi.org/10.1002/adma.202003021.

39. Augustyn, V., Come, J., Lowe, M.A., Kim, J.W., Taberna, P.L., Tolbert, S.H., Abruña, H.D., Simon, P., and Dunn, B. (2013). High-rate electrochemical energy storage through Li+ intercalation pseudocapacitance. Nat. Mater. *12*, 518–522. https://doi.org/10.1038/nmat3601.

40. Wang, S., Yuan, Z., Zhang, X., Bi, S., Zhou, Z., Tian, J., Zhang, Q., and Niu, Z. (2021). Non-metal ion Co-insertion chemistry in aqueous Zn/MnO2 batteries. Angew. Chem. Int. Ed. Engl. *60*, 7056–7060. https://doi.org/10.1002/anie.202017098.

41. Lou, G., Pei, G., Wu, Y., Lu, Y., Wu, Y., Zhu, X., Pang, Y., Shen, Z., Wu, Q., Fu, S., and Chen, H. (2021). Combustion conversion of wood to N, O co-doped 2D carbon nanosheets for zinc-ion hybrid supercapacitors. Chem. Eng. J. *413*, 127502. https://doi.org/10.1016/j.cej.2020.127502.

42. Wang, S., Wang, Q., Zeng, W., Wang, M., Ruan, L., and Ma, Y. (2019). A new free-standing aqueous zinc-ion capacitor based on MnO2-CNTs cathode and MXene anode. Nano-Micro Lett. *11*, 70. https://doi.org/10.1007/s40820-019-0301-1.

43. Cui, F.-Z., Liu, Z., Ma, D.-L., Liu, L., Huang, T., Zhang, P., Tan, D., Wang, F., Jiang, G.-F., and Wu, Y. (2021). Polyarylimide and porphyrin based polymer microspheres for zinc ion hybrid capacitors. Chem. Eng. J. *405*, 127038. https://doi.org/10.1016/j.cej.2020.127038.

44. Patil, S.J., Chodankar, N.R., Hwang, S.-K., Raju, G.S.R., Ranjith, K.S., Huh, Y.S., and Han, Y.-K. (2022). Ultra-stable flexible Zn-ion capacitor with pseudocapacitive 2D layered niobium oxyphosphides. Energy Storage Mater. *45*, 1040–1051. https://doi.org/10.1016/j.ensm.2021.10.040.

45. Zhang, Y., Wang, Z., Li, D., Sun, Q., Lai, K., Li, K., Yuan, Q., Liu, X., and Ci, L. (2020). Ultrathin carbon nanosheets for highly efficient capacitive K-ion and Zn-ion storage. J. Mater. Chem. *8*, 22874–22885. https://doi.org/10.1039/d0ta08577d.

46. Wan, C., Jiao, Y., Liang, D., Wu, Y., and Li, J. (2018). A high-performance, all-textile and spirally wound asymmetric supercapacitors based on core–sheath structured MnO2 nanoribbons and cotton-derived carbon cloth. Electrochim. Acta *285*, 262–271. https://doi.org/10.1016/j.electacta.2018.07.036.

47. Lu, Y., Li, Z., Bai, Z., Mi, H., Ji, C., Pang, H., Yu, C., and Qiu, J. (2019). High energy-power Zn-ion hybrid supercapacitors enabled by layered B/N Co-doped carbon cathode. Nano Energy *66*, 104132. https://doi.org/10.1016/j.nanoen.2019.104132.

STAR★METHODS

KEY RESOURCES TABLE

REAGENT or RESOURCE	SOURCE	IDENTIFIER
Chemicals, peptides, and recombinant proteins		
Zinc sulfate heptahydrate ($ZnSO_4 \cdot 7HO_2$)	Aladdin	CAS: 7733-02-0
Gelatins	Aladdin	CAS: 9000-70-8
Potassium hydroxide (KOH)	Aladdin	CAS: 1310-58-3
boric acid (H_3BO_3)	Aladdin	CAS: 10043-35-3
Sodium sulfate anhydrous (Na_2SO_4)	Aladdin	CAS: 7757-82-6
Software and algorithms		
Origin 2018	OriginLab	https://www.originlab.com
3ds Max 2018	Autodesk	https://www.autodesk.com
Photoshop 2020	Adobe	https://www.adobe.com

RESOURCE AVAILABILITY

Lead contact

Further information and requests for resources and reagents should be directed to and will be fulfilled by the lead contact, Caichao Wan (wancaichaojy@163.com).

Materials availability

This study did not generate new unique reagents.

Data and code availability

- Original data reported in this paper will be shared by the lead contact upon request.
- This paper does not report original code.
- Any additional information required to reanalyze the data reported in this paper is available from the lead contact upon request.

METHOD DETAILS

Preparation of CFs

The Fabrication of CFs was carried out by transferring the clean and dried jean samples (100% cotton, 20 × 40 cm^2) into a tubular furnace equipped with a quartz tube (80 mm in diameter) for pyrolysis under a flow of N_2 (99.999%) with 100 sccm rate. The samples were heated to 1000 °C at a heating rate of 5 °C min^{-1}, and this temperature was maintained for 4 h to allow for complete pyrolysis; subsequently, the furnace decreased naturally to room temperature.

Preparation of GNSs@CFs and N–GNF@CFs

GNSs were synthesized on the surface of CFs substrate (area: 4 × 2 cm^2, mass: 16.4 mg cm^{-2}) by using a radio-frequency plasma-enhanced chemical vapor deposition facility (RF–PECVD, BTF–1200C–II–SL, Best Equipment Technology Co., Ltd). Firstly, a vacuum (5 Pa) is created inside of reaction chamber, then Ar gas (80 Sccm) was injected into the chamber (a quartz tube with 80 mm in diameter) and the CFs substrate was heated up to 800 °C at a heating rate of 30 °C min^{-1}. Subsequently, the CH_4 gas (20 Sccm) was injected into the chamber and the RF plasma is activated at 200 W radio waves with the reaction pressure of 200 Pa. The reaction lasted for 120 min and then was cooled down naturally. The mass loading of GNSs was determined to be ≈0.6 mg cm^{-2} by using gravimetric difference between the CFs and GNSs@CFs. Similarly, N–GNF@CFs was fabricated by using GNSs@CFs as the precursor. Specifically, in a condition of N_2 gas flow (50 Sccm), GNSs@CFs is treated in the pure N_2 plasma which is instigated at 500 W radio waves. Different durations (5, 10, and 20 min) of the N_2 plasma activation were carried out. The obtained samples in different treatment durations were denoted as N–GNF@CFs–*x*, (*x* = 5, 10, 20). Unless otherwise specified, N–GNF@CFs refers to N–GNF@CFs–10.

Preparation of the flexible quasi-solid-state ZIC

The ZnNSs@CFs anode was first fabricated by a typically electrochemical deposition technology. The $ZnSO_4$/gelatin gel electrolyte was prepared by mixing 10 mL 1 M $ZnSO_4$ solution and 1 g gelatin grains at 80°C until the mixture becomes transparent. N–GNF@CFs cathode, Zn NSs@CFs anode, and a piece of cellulose paper were dipped in the $ZnSO_4$/gelatin solution for 10 min at 80°C to allow the permeation of electrolyte into the internal electrode. After scraping superficial excess electrolyte, the electrodes were cooled down to room temperature. Finally, a sandwich-like flexible device was successfully assembled by using N–GNF@CFs cathode, Zn NSs@CFs anode, and $ZnSO_4$/gelatin gel electrolyte coupling with a cellulose separator.

Material characterizations

The morphology of the samples was observed using a transmission electron microscope (TEM) (FEI, Tecnai G2 F20) and a scanning electron microscope (SEM) (Hitachi, S4800) equipped with an Energy Dispersive X–Ray (EDX) spectroscopy detector for elemental analysis. Pore distribution and SSA were analyzed by N_2 adsorption-desorption tests by an accelerated surface area and porosimeter system (3H–2000PS2 unit, Beishide Instrument S&T Co., Ltd). X–ray diffraction (XRD) analysis was implemented on a Bruker D8 Advance TXS XRD instrument with Cu Kα (target) radiation (λ = 1.5418 Å) at a scan rate (2θ) of $4° \ min^{-1}$ and a scan range from 5 to 90°. Raman spectra were recorded using a Renishaw InVia micro-Raman system with an excitation wavelength of 514 nm. X–ray photoelectron spectroscopy (XPS) was performed on a Thermo Escalab 250Xi system using a spectrometer with a dual Al Ka X–ray source.

Electrochemical characterizations

Electrochemical properties of electrodes were firstly investigated in a three-electrode system with Hg/HgO and Pt sheet as the reference and counter electrodes, respectively, in 3 M KOH aqueous electrolyte. Electrochemical impedance spectroscopy was carried out at open circuit potential in a frequency range from 0.05 Hz to 40 kHz with a perturbation of 10 mV. The electrochemical performance of the quasi-solid-state ZIC was evaluated by a two-electrode testing system. All electrochemical measurements were carried out on a multichannel electrochemical analyzer (Wuhan CorrTest Instruments Co., Ltd, China).

Calculations

In the three-electrode system, the areal (C_s, F cm^{-2}) and gravimetric (C_m, F g^{-1}) are calculated from the GCD curves at various current densities according to the following equations:[46]

$$C_s = \frac{I \times \Delta t}{\Delta V \times s} \quad \text{(Equation 5)}$$

$$C_m = \frac{I \times \Delta t}{\Delta V \times m} \quad \text{(Equation 6)}$$

Where I, Δt, and ΔV refer to the constant discharge current (mA), discharge time (s), and potential window (V), respectively. s and m represent the specific area (cm^2) and mass (mg) of the electrodes, respectively. The specific capacity (C, mAh g^{-1}) for the ZIC device was precisely determined through the discharge curve by the equation below:[47]

$$C = 2I \int V dt / 3.6m \quad \text{(Equation 7)}$$

where I (A), ∫ Vdt (Vs), V (V) and m (g) represent the discharge current (A), the integral area under discharge curve, the voltage after ohmic drop, and the mass of active material in cathode, respectively. The energy density (E, Wh kg^{-1}) and power density (P, W kg^{-1}) for the ZIC devices were calculated based on the mass of active material in cathode by the equations below:[47]

$$E = I \int V dt / 3.6m \quad \text{(Equation 8)}$$

$$P = 3600E/I \quad \text{(Equation 9)}$$

QUANTIFICATION AND STATISTICAL ANALYSIS

Quantification and statistical analysis were performed by Origin 2019.